Deep Prior Based Limited-Angle Tomography

D. M. Bappy[1], Donghwa Kang[1], Jinkyu Lee[2], Youngmoon Lee[3], and Hyeongboo Baek[4(✉)]

[1] Department of Computer Science and Engineering, Incheon National University, Incheon, Republic of Korea
[2] Department of Computer Science and Engineering, Sungkyunkwan University, Suwon, Republic of Korea
[3] Department of Robotics, Hanyang University, Ansan, Republic of Korea
[4] Department of Artificial Intelligence, University of Seoul, Seoul, Republic of Korea
hbbaek359@gmail.com

Abstract. In the process of reconstructing images from data acquired within a limited angular range, we encounter what is termed limited-angle tomography. The deficiency of complete data in this context results in artifacts, commonly appearing as streaks or missing structures, which can significantly compromise the quality of the reconstructed slice. This degradation gives rise to issues such as boundary distortion, blurred edges, and intensity bias, potentially leading to misinterpretation of the images. Hence, addressing artifacts in limited-angle tomography is crucial for clinical applications. Although deep learning-based reconstruction has shown impressive results in recent times, concerns about its robustness persist. To bolster the robustness of our proposed technique, we integrate prior information from a modified U-net with preprocessed input into the Relative Variation - Simultaneous Algebraic Reconstruction Technique (RV-SART) to provide insights into unmeasured data. Subsequently, the method extracts structure from the initially reconstructed slice through structure-texture decomposition. This process facilitates the reconstruction of high-quality CT images while suppressing pattern-like artifacts. Extensive experiments demonstrate that our approach surpasses both traditional and state-of-the-art learning techniques in terms of reconstruction quality and preservation of fine structures in noisy limited-angle reconstruction problems. Our technique provides improvements over the recent LRIP-net for a 90-degree scanning range in quantitative metrics such as PSNR by 17.48%, RMSE by 46.36%, and SSIM by 6.18%.

Keywords: Limited Angle Tomography · Deep Prior · Artifacts.

1 Introduction

Computed Tomography (CT) finds applications in diverse fields, including medical examinations [13] [18], industrial nondestructive testing [16], and security

inspection [14]. In the context of medical CT, increasing attention is being devoted to mitigating X-ray radiation doses due to their potential harm to patients [15]. The reduction of radiation dose holds practical significance for patient well-being. Strategies for achieving this objective include lowering the X-ray tube current or decreasing the number of projection views. For instance, a straightforward and effective approach is limited-angle CT scanning, where projection views are constrained to a specific angular range. Limited-angle CT scanning is encountered not only in medical applications but also in scenarios such as the nondestructive testing of pipelines in service [31]. In this context, the scanning environment necessitates CT scanning within a restricted angular range. Furthermore, limited-angle CT scanning is employed to enhance temporal resolution in coronary computed tomography angiography [7]. Within micro-CT applications, certain identified objects exhibit distinctive structures, including elongated and discoid shapes. In such cases, the object's rotational range is constrained due to limitations in imaging geometry. Alternatively, in specific projection views, complete X-ray absorption occurs, leading to projection loss [29]. In summary, limited-angle CT has garnered increasing attention in recent years.

The rise of Convolutional Neural Networks (CNNs) across various computer vision tasks has led to a growing popularity of deep learning approaches in the field of medical imaging. Pelt and Batenburg [26] introduced an artificial neural network-based algorithm for fast limited-angle image reconstruction. This method is essentially a weighted combination of the Filtered Back Projection (FBP) technique and learned filters. Boublil et al. [5] applied a CNN-based model to integrate multiple reconstructed results, while Kang et al. [22] developed a deep CNN model in the wavelet domain, training wavelet coefficients from CT images using the contourlet transform. While the aforementioned approaches have shown promising outcomes and notably enhanced the quality of reconstructed images, certain limitations persist. One drawback is the absence of guaranteed worst-case performance from these algorithms. Another limitation is their reliance on post-processing methods, overlooking data consistency.

It is evident that iterative methods and learning-based methods exhibit a primary distinction. The former demonstrates flexibility in addressing diverse information retrieval tasks by straightforwardly specifying parameters and optimization. Conversely, the latter necessitates laborious training to acquire knowledge of the model before testing and typically faces limitations tied to specialized tasks. The practical implementation of deep learning techniques in limited-angle tomography faces significant challenges attributed to two major factors: First, the potential lack of generalization to unseen data due to inadequate training data; and second, sensitivity to noise. Consequently, images reconstructed solely through deep learning methods may appear suboptimal. Additionally, we observe that limited-angle reconstruction consists of pattern-like artifacts, causing small structures to be invisible. This issue can be resolved if we can separate structure and texture from the reconstructed slice.

We propose a hybrid approach that combines deep learning with iterative reconstruction. The objective is to leverage Relative Variation - Simultaneous Algebraic Reconstruction The technique (RV-SART) to impose constraints on the reconstructed images, ensuring consistency with the measured projection data, while unmeasured information is supplemented as prior information from FBPConvNet with preprocessed input. To achieve this, we introduce a method known as Deep Prior Based RV-SART. Firstly, we employ the Simultaneous Algebraic Reconstruction Technique - Total Variation (SART-TV) using limited-angle data. Following this, the resulting reconstructed output is input into the CNN to extract details about unmeasured data. In the subsequent phase, the output from the CNN is incorporated into RV-SART, providing crucial prior information. In this stage, the initially reconstructed slice undergoes decomposition into structure-texture components, aiding in the extraction of structural information and the mitigation of pattern-like artifacts. This process guarantees the reconstruction of high-quality CT images.

In Figure 4, we showcase the application of our proposed reconstruction technique alongside a recent learning-based approach. The visual representation illustrates the effective suppression of artifacts and the highly accurate reconstruction of intricate structures achieved by our method. Substantiating these visual results, we present a comparative analysis using three key quantitative metrics in Table 1. This table reveals remarkable enhancements, including a 17.48% increase in PSNR, a 46.36% reduction in RMSE, and a 6.18% improvement in SSIM when compared to the second-best performance listed in the table.

2   Related work

Numerous academics have pondered the limitations of post-processing approaches and have shifted their focus towards emphasizing data consistency to enhance the quality of reconstructed images. Certain methods leverage neural networks to incorporate prior information into existing iterative reconstruction algorithms [1,3,8,17]. Specific approaches, as described in references [6,9,10,20,24,33] embrace an end-to-end strategy that suggests the unfolding of an iterative algorithm and comprehensive training as a deep neural network. This approach facilitates the integration of physical information into the architecture through data consistency blocks, which are combined with trainable CNN regularizers.

DIOR [20] is a recent technique that employs a hybrid approach in the residual domain. In contrast, our hybrid approach operates in the image domain. Our method is simpler architecture and more effective in reconstructing high-quality CT images, with lower computational complexity compared to DIOR. According to our straightforward hybrid technique, structure-texture decomposition proves to be more effective compared to separating high and low-frequency components. This is because we deliberately extract texture components as pattern-like noise using relative variation, and then successfully remove them from the reconstructed CT images.

The technique we propose utilizes prior information that falls within the realm of deep learning-based reconstruction, specifically categorized as image-to-image reconstruction. In this approach, direct access to raw measurements is not necessary, indicating that image reconstruction is independent of manufacturing protocols. Through the utilization of a CNN, our method effectively maps low-quality images to their high-quality counterparts without requiring additional inputs. In the domain of post-processing sparse-view CT reconstruction, CNN plays a pivotal role, with FBPConvNet [21] standing out as a notable representative. FBPConvNet adopts the FBP algorithm for image reconstruction and integrates a CNN structure based on U-Net [27] for image segmentation that includes both an encoder and a decoder. Notably, FBPConvNet introduces a skip connection between the input and output, enhancing the network's ability to discern subtle distinctions. To address the limitations of U-Net, Han et al. [19] introduced Framing U-Net as an alternative post-processing method, specifically tailored to meet frame conditions. Another innovative approach comes from Lee et al. [23], who employed a multi-level wavelet U-Net, showcasing superior results compared to traditional U-Net. Despite the significant success of these post-processing techniques, it is crucial to note that they do not incorporate sinogram information into their CNN architectures. As a result, in extremely ill-posed problems where there are very limited numbers of projections, the aforementioned networks fail to reconstruct high-quality CT images and suppress artifacts.

Limited-angle geometry   SART-TV Reconstruction
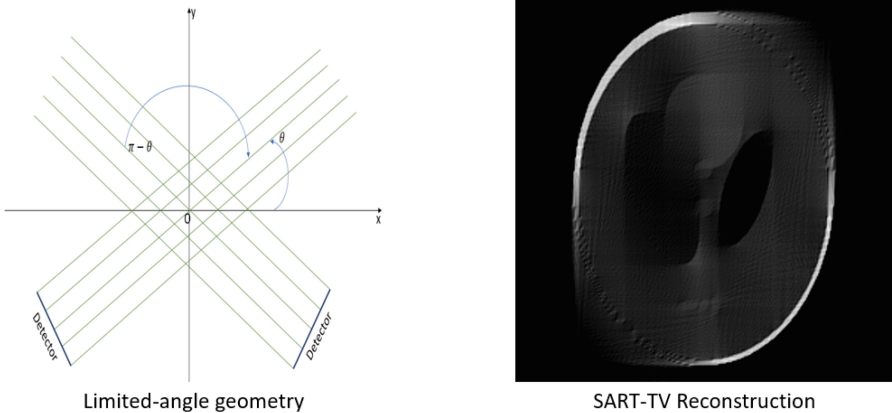
Fig. 1. Limited-angle parallel-beam scanning configuration

3   Approach

We examine the limited-angle parallel-beam CT in a two-dimensional setting. Figure 1 depicts the scanning configuration for this limited-angle parallel-beam

CT. Additionally, the initial reconstruction for the limited angle with a straightforward phantom model is presented in Figure 1. The reconstruction reveals artifacts, boundary distortion, and structure loss attributed to the insufficient number of projections obtained through limited-angle scanning.

3.1 Deep Prior Estimation

Jin et al. [21] introduced a post-processing image reconstruction technique named FBPConvNet, utilizing the FBP method to reconstruct the initial slice from sparse data and feed it into the CNN input layer. This approach exhibited impressive results in addressing sparse-view reconstruction in parallel beam X-ray CT.

FBPConvNet uses Filtered Back Projection (FBP) and a modified U-net for the reconstruction of sparse-view CT scans. The FBP reconstructs CT images using the available sparse projection data. Due to the incompleteness of the available data, artifacts are present in the reconstruction. To address this issue, the reconstructed CT scans from sparse views undergo training with a modified U-net, using full-view CT scans as the labeled images, aiming to eliminate the artifacts. The modified U-net incorporates two modifications. Firstly, zero padding is applied to ensure that the image size remains constant after each convolution. Secondly, the final layer is substituted with a convolutional layer, reducing the 64 channels to a singular output image. While this approach proved successful for sparse data, it encounters challenges in reconstructing data from a limited scan range. In such cases, artifacts not only encompass pattern-like noise but also involve boundary distortion. The FBP technique struggles to effectively reconstruct distorted boundaries. In contrast, the SART-TV method excels in reconstructing the initial boundary and effectively reducing noise from limited data when compared to FBP.

Building on their work, we leverage the SART-TV method to compute the initial slice and then insert it into the modified U-net input layer, specifically for limited-angle CT reconstruction. The rationale behind this choice lies in the superior performance of the SART-TV method when dealing with incomplete data, resulting in a higher-quality training set compared to the FBP. Considering the importance of training set quality in the modified U-net, this contributes to an enhanced efficacy for limited-angle reconstruction.

Our proposed method comprises the following steps: Firstly, we apply the SART-TV method to limited-angle projection data obtained from the LDCT dataset. Subsequently, we input the slice reconstructed by the SART-TV method into the modified U-net trained to minimize the disparity between the reconstructed image and the labeled image.

3.2 Initial Reconstruction

We utilize the discrete linear model for CT imaging:

$$\boldsymbol{Af} = \boldsymbol{p} \tag{1}$$

where A is the system matrix, p is the vector of measured projection data, and f is the image to be reconstructed.

Our goal is to reconstruct f satisfying the following constraint:

$$\| \, \boldsymbol{A}\boldsymbol{f} - \boldsymbol{p} \, \| < \mu \tag{2}$$

where μ is a parameter representing error tolerance. In the noise-free case, μ is ideally zero, while in the noisy case, it is set to a positive value.

Due to the severe ill-posedness of limited-angle tomography, the number of images satisfying the above constraint is not unique. We aim to reconstruct an image that satisfies this constraint and is simultaneously close to the modified U-net reconstruction $\boldsymbol{f}_{prior}$. To achieve this, we choose to initialize the reconstruction $\boldsymbol{f}$ iteratively, starting with $\boldsymbol{f}^{(0)} = \boldsymbol{f}_{prior}$, and solving it as follows:

$$\| \, \boldsymbol{A}\boldsymbol{f} - \boldsymbol{p} \, \| < \mu \quad and \quad \boldsymbol{f}^{(0)} = \boldsymbol{f}_{prior} \tag{3}$$

Reconstructed slice $\boldsymbol{f}$ is computed as:

$$\boldsymbol{f}_j^{t+1} = \boldsymbol{f}_j^t + \gamma \cdot \frac{\sum_{\boldsymbol{p}_i \epsilon \boldsymbol{P}_\alpha} \frac{S_\epsilon \left(\boldsymbol{p}_i - \sum_{k=1}^M \boldsymbol{A}_{i,k} \cdot \boldsymbol{f}_k^l\right)}{\sum_{k=1}^M \boldsymbol{A}_{i,k}} \boldsymbol{A}_{i,j}}{\sum_{\boldsymbol{p}_i \epsilon \boldsymbol{P}_\alpha} \boldsymbol{A}_{i,j}}, \tag{4}$$

where i represents the projection ray index of p, j denotes the pixel index of f, $\boldsymbol{A}_{i,j}$ signifies the element of matrix $\boldsymbol{A}$ at the i-th row and j-th column, M stands for the total number of pixels, t denotes the iteration number, α represents the X-ray source rotation angle, γ is a relaxation factor typically set to 0.7, and $\boldsymbol{P}_\alpha$ denotes the set of projection rays corresponding to the X-ray source rotation angle α and S_ϵ denotes soft-thresholding operator with threshold ϵ.

3.3   Structure-Texture Decomposition

Subsequently, we engage in structure-texture decomposition for the reconstructed slice $\boldsymbol{f}$ to eliminate artifacts. We employ the concept of Relative Variation (RV) [30] to distinguish and extract structure and texture from the reconstructed slice. The expression for the RV of the reconstructed slice is as follows:

$$arg \ min \sum_{pix} (\boldsymbol{S}_{pix} - \boldsymbol{f}_{pix})^2 + \lambda \cdot \left(\frac{D_x(pix)}{L_x(pix) + \varepsilon} + \frac{D_y(pix)}{L_y(pix) + \varepsilon} \right) \tag{5}$$

$\boldsymbol{S}$ represents the resulting structure image. The term $(\boldsymbol{S}_{pix} - \boldsymbol{f}_{pix})^2$ serves to stabilize the input and output, preventing wild deviations. The regularizer, denoted as relative total variation (RTV), accounts for the impact of texture removal in an image. This regularizer is defined as $\left(\frac{D_x(pix)}{L_x(pix)+\varepsilon} + \frac{D_y(pix)}{L_y(pix)+\varepsilon} \right)$, where λ in Equation (5) represents a weighting factor, and ε is a small positive number crucial for preventing division by zero in the element-wise operation. D is the pixel-wise windowed total variation in horizontal and vertical directions, and L denotes the windowed inherent variation that captures the overall spatial

variation. The solution of the loss function aims to make the extracted structures similar to those in the input image, while L and D provide information about the texture part. Textures, being the pattern-like effects, are undesirable in the CT image. Therefore, we will utilize D computed from Equation (5) to remove the pattern-like noise in our proposed RV-SART algorithm.
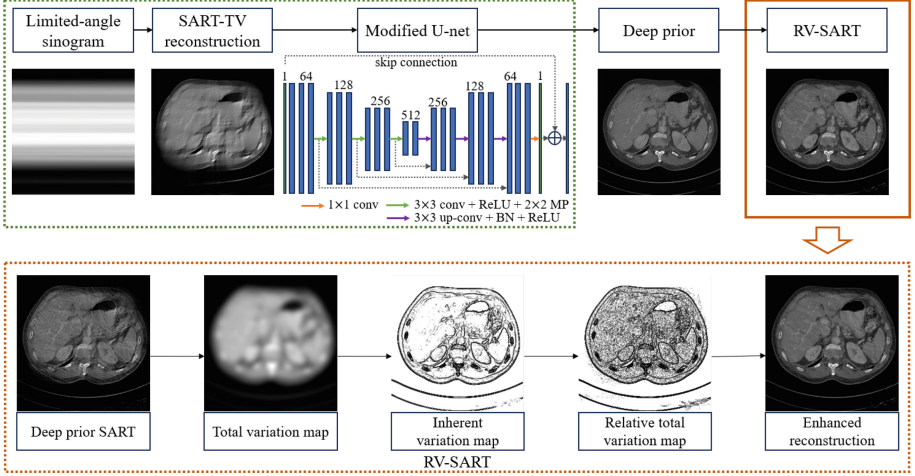

Fig. 2. Schematic of the proposed technique

3.4 Limited-Angle Reconstruction Algorithm

Figure 2 delineates our proposed methodology, providing a comprehensive overview of each section's output. In this figure, the reconstruction process part shows the overall reconstruction process, which includes two main parts: modified U-net with preprocessed input and RV-SART.

The first part shows the CNN model based on the U-net. It is composed of an encoder path and a decoder path. The encoder path consists of numerous 3×3 convolutions, rectified linear units, and 2×2 max pooling operations represented in the green arrow. The decoder path also consists of numerous 3×3 up-convolutions, batch normalizations, and rectified linear units represented in the purple arrow. The skip connection and the concatenation in the black dashed line arrow are available because of the loss of useful information in every convolution and max pooling. In the final layer of the CNN, a 1×1 convolution represented in an orange arrow is used to make the CNN output a single-channel image, which is the final reconstructed image.

RV-SART receives the CNN output and uses it as prior information about unmeasured data during reconstruction for data consistency with the measured data. During this stage, the initially reconstructed slice undergoes decomposition

---

Algorithm 1 Deep Prior Based RV-SART

`Parameter initialization`

1: $\lambda = 0.0002, \sigma = 5, \eta = 15, k = 4$;

`Prior reconstruction`

2: $\boldsymbol{f}_{prior}$ = initial reconstruction from modified U-net with preprocessed input

---

3: $\boldsymbol{f} = \boldsymbol{f}_{prior}$

4: $\boldsymbol{f}_0 = \boldsymbol{f}$

    `Relative Variation SART`

5: **for** $i = 1 : N_d$ **do**

6:     $\boldsymbol{f} = \boldsymbol{f} + \lambda A_i \frac{\boldsymbol{p} - A_i \boldsymbol{f}}{A_i . A_i}$

7:     $\boldsymbol{f}_{fil} = median_{filter}(\boldsymbol{f})$

    `Enforce positivity`

8:     **if** $\boldsymbol{f}_i < 0$ **then**

9:         $\boldsymbol{f}_i = 0$

10:    **end if**

11:    $\boldsymbol{S}_0 = \boldsymbol{f}$

    `Structure-Texture decomposition`

12:    solve $D_x, D_y, L_x, L_y, \boldsymbol{S}_{pix}$ using [33]

13:    **return** $D_x, D_y, \boldsymbol{S}_{pix}$

    `Enhance Reconstructed slice structure`

14:    $\boldsymbol{f} = \boldsymbol{S}_{pix}$

15:    $\boldsymbol{f}_{en} = \boldsymbol{f} - (D_x + D_y)$

16:    $\boldsymbol{p} = A\boldsymbol{f}_{en}$

    `compute` l^2 `norm`

17:    $N_i = \sqrt{\boldsymbol{p} - A\boldsymbol{f}_{en}}$

    `until {stopping criteria}`

18:    **if** $i \neq 1 \&\& N_i > N_{i-1}$ **then**

19:       **return** $\boldsymbol{f}_{en}$

20:    **end if**

21: **end for**

22: **return** $\boldsymbol{f}_{en}$

---

into structure-texture components through total variation and inherent variation, as shown in the RV-SART stage, facilitating the extraction of structural information and the suppression of pattern-like artifacts. This comprehensive process ensures the generation of high-quality CT images.

Considering the lower dose used to obtain the measured data introduces inherent noise. To mitigate this, we apply a small-sized filter according to the following expressions:

$$\boldsymbol{f} = \boldsymbol{f}_{prior} + \gamma A_i \frac{\boldsymbol{p} - A_i \boldsymbol{f}}{A_i . A_i} \tag{6}$$

$$\boldsymbol{f}_{fil}(s, t, v) = median\{\boldsymbol{f}(s + l, t + m, v + n) | (l, m, n) \epsilon R\} \tag{7}$$

Subsequent observations reveal artifacts in the reconstructed slice due to the significant amount of incomplete data. These artifacts exhibit a pattern resem-

bling stripes. To address this, we employ a structure-texture decomposition to separate pattern-like artifacts from the structure and enhance the reconstructed slice as expressed in Equation 5:

$$\boldsymbol{f}_{en} = \boldsymbol{f} - (D_x + D_y) \tag{8}$$

Algorithm 1 outlines the Deep Prior Based RV-SART in pseudocode. The process begins with the initialization of parameters in the parameter initialization phase (Line 1). Subsequently, the initial reconstruction is computed using a modified U-net with preprocessed input and established as a prior (Lines 2-3) to address the unmeasured region. The RV-SART phase (Lines 4-21) delineates the key steps involved in ensuring consistency between the unmeasured data and the measured projection data. The initially reconstructed slice, denoted as $\boldsymbol{f}_0$, acts as a temporary variable throughout the reconstruction process. An initial slice is reconstructed using prior information, and a small filter is employed to suppress noise while maintaining data consistency and positivity (Lines 5-10). The initially reconstructed slice is then assigned to the temporary variable $\boldsymbol{S}_0$ for further processing. To mitigate pattern-like artifacts stemming from limited data, structure-texture decomposition is performed on the reconstructed slice (Lines 11-13). The resulting slice, with suppressed pattern-like artifacts, becomes the current reconstructed slice, and its brightness is enhanced by subtracting windowed total variation (Lines 14-15). Subsequently, a forward projection is computed using the enhanced reconstructed slice, and the l^2 norm is calculated (Lines 16-17). The algorithm verifies the convergence criteria (Line 18). Finally, the high-quality CT slice is obtained (Line 22).

4   Experiments

Dataset. We employ the clinical dataset from the 2016 AAPM Low-Dose CT (LDCT) Grand Challenge [25], provided by the Mayo Clinic. We create the projection data within a parallel-beam geometry system using Siddon's ray-driven algorithm [28]. This dataset is already infused with realistic noise. Furthermore, we introduced a 10% Gaussian noise for comparison with state-of-the-art techniques.

Implementation. We employed a training dataset comprising 2 patient records from the AAPM dataset, and for testing, we employed data from a separate patient within the same AAPM dataset. The training process for modified U-net involved using pairs of limited-view SART-TV slices as input and full-view SART-TV slices as label. The limited-view SART-TV slices were computed from three distinct scanning angular ranges: 90, 120, and 150 degrees. In contrast, the full-view SART-TV slices were computed using the full 360-degree angular range. It is crucial to emphasize that this training approach makes the method applicable to real CT reconstructions, where access to an oracle reconstruction is unavailable. Following this, the network's output is fed into the iterative
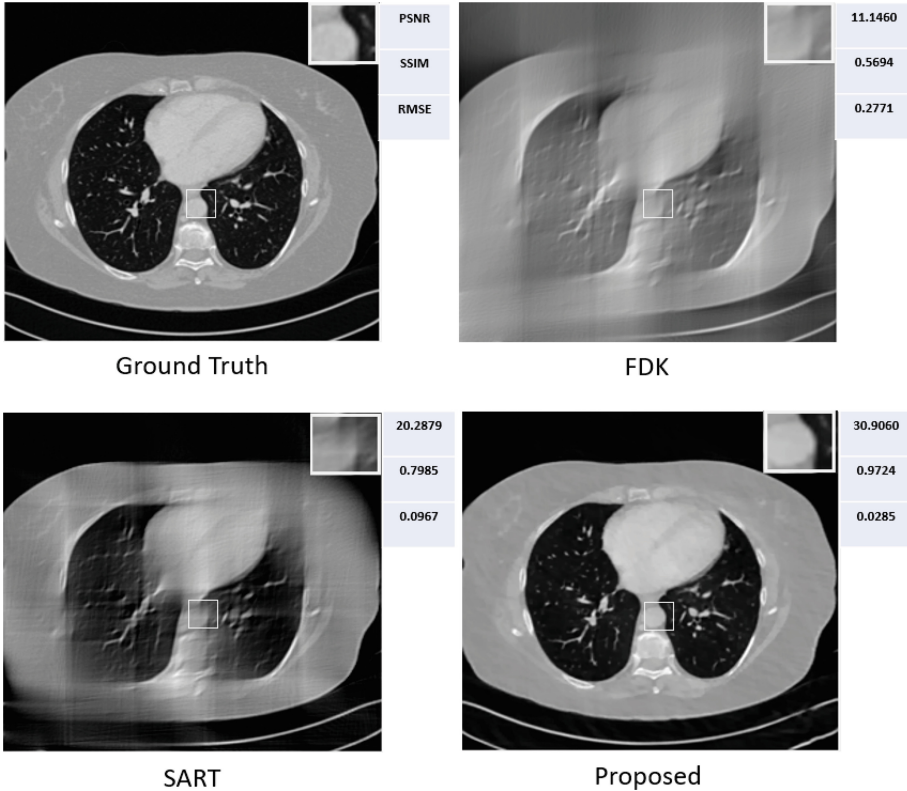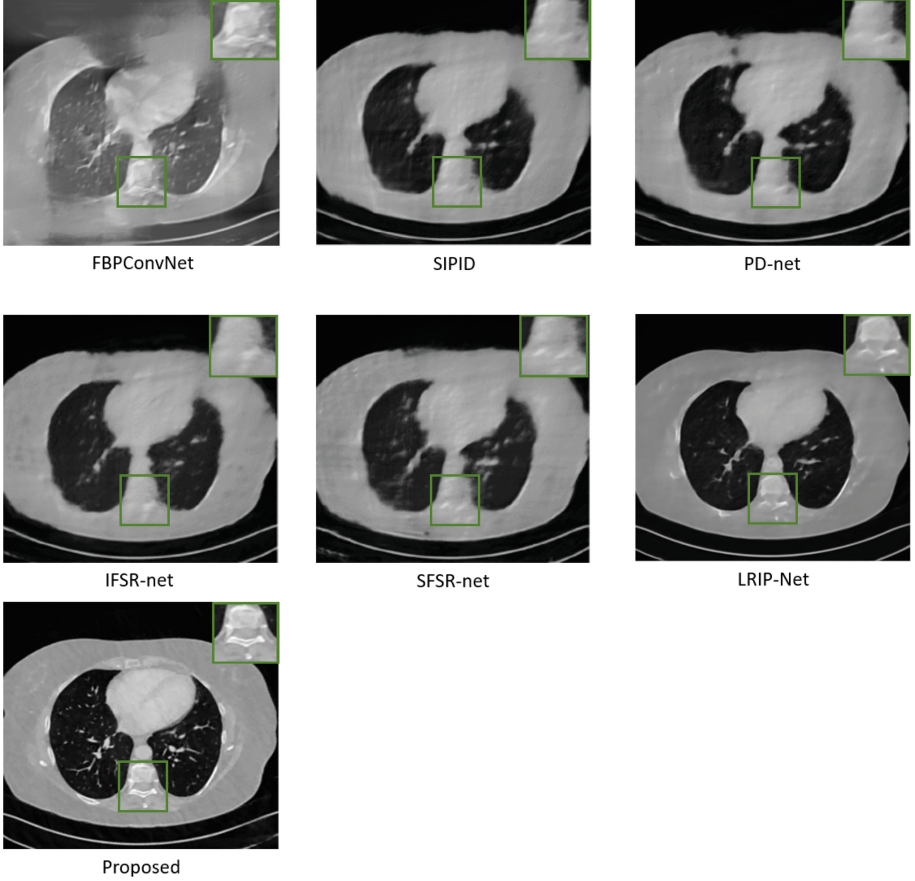
Fig. 3. Limited-angle reconstruction experiment of the AAPM dataset with 90° scanning angular range

model RV-SART as prior information for high-quality reconstruction. This process ensures accurate reconstruction of the structure while effectively suppressing artifacts. This limited-view reconstruction holds significant relevance in human imaging, as a substantial reduction in the number of views, for instance, a specific number of decrease in projections, corresponds to an equivalent reduction in the radiation dose administered to the patient.

Baseline methods. We compare two widely used classical techniques and six state-of-the-art learning-based techniques as our baselines, including traditional methods FDK [11] and SART [2], learning based methods FBPConvNet [21], LRIP-Net [12], SIPID [32], PD-net [1], IFSR-net [9], and SFSR-net [9]. To ensure a fair comparison, we employ parallel geometry for all techniques and apply the 2D network for slice-wise reconstruction.

Evaluation metrics. We assess the reconstructed CT slice using three quantitative metrics, namely peak signal-to-noise ratio (PSNR), structural similarity

(SSIM), and root-mean-square error (RMSE), following prior studies in [4]. Superior reconstruction quality is indicated by higher PSNR/SSIM values and lower RMSE values.

Fig. 4. Comparing Learning-Based Techniques for Limited-Angle Reconstruction Experiment to Preserve Structural Integrity in the AAPM Dataset with a 90° Scanning Angular Range

4.1 Results

Qualitative Evaluation. Figure 3 illustrates both the qualitative and quantitative performance of our proposed technique in comparison to frequently used traditional methods using the AAPM dataset with a 90-degree scanning angular range. In the reconstruction, it is evident that FDK completely failed to reconstruct the structure. SART performs reasonably well in reconstructing the region

Table 1. Evaluating Limited-Angle Data Distorted by 10% Gaussian Noise: A Comparative Analysis based on PSNR, RMSE, and SSIM Metrics

Noise	N_{view}	Method	PSNR	RMSE	SSIM
10%	150	FBPConvNet	21.8293	0.0810	0.7887
		SIPID	29.0276	0.0345	0.9193
		PD-net	29.0084	0.0354	0.9193
		SFSR-net	29.4543	0.0336	0.9199
		IFSR-net	29.6694	0.0328	0.9231
		LRIP-Net	30.8026	0.0288	0.9362
		Proposed	**31.6783**	**0.0261**	**0.9800**
	120	FBPConvNet	20.0065	0.0999	0.7465
		SIPID	26.6271	0.0461	0.8941
		PD-net	26.7667	0.0458	0.8944
		SFSR-net	27.2079	0.0436	0.9034
		IFSR-net	27.2853	0.0432	0.9032
		LRIP-Net	29.1261	0.0349	0.9256
		Proposed	**31.5577**	**0.0264**	**0.9740**
	90	FBPConvNet	18.7582	0.1153	0.7252
		SIPID	23.6216	0.0664	0.8607
		PD-net	23.6473	0.0657	0.8615
		SFSR-net	23.7253	0.0651	0.8591
		IFSR-net	24.2056	0.0616	0.8701
		LRIP-Net	25.9377	0.0457	0.9141
		Proposed	**30.9060**	**0.0285**	**0.9724**

with available data but struggles in areas with unavailable data. In comparison, our proposed technique demonstrates excellent performance in reconstructing fine structures and suppressing artifacts, particularly within the delineated white box. These qualitative results align closely with the quantitative values, as observed from significantly lower values in comparison to our proposed technique.

Figure 4 illustrates the outcomes of the reconstruction achieved by very recent learning-based approaches in the context of 90° limited-angle reconstruction. It is evident that learning-based methods demonstrate successful reconstruction in the missing angular region compared to classical techniques.

To thoroughly assess the preservation of structure and the removal of artifacts, we selected a small yet intricate feature within the image slice, demarcated by a green box. The FBPConvNet falls short in reconstructing even the outer structure of the slice, as it was expressly designed for sparse data and struggles to reconstruct adequately from limited input.

In comparison, SIPID [32], PD-net [1], IFSR-net [9], and SFSR-net [9] demonstrate commendable performance in reconstructing the overall structure. However, they still face challenges in accurately reconstructing small structures, and a significant portion of fine details is lost during the noise suppression process.

Conversely, LRIP-Net [12] exhibits proficient reconstruction of the majority of structures, yet struggles with the precise reconstruction of small features. In contrast, our proposed technique excels in reconstructing almost all fine structures flawlessly. This success is attributed to our approach of implementing structure-texture decomposition in the initial reconstruction phase, effectively eliminating pattern-like artifacts from the overall structure.

Notably, our proposed technique showcases superior preservation of image details and edges, as emphasized in the magnified region within the green box.

Quantitative Evaluation. Table 1 presents quantitative metrics for comparing recent learning-based techniques with our proposed approach. The evaluation encompasses three distinct limited-angle scanning configurations, each subjected to an additional 10% of Gaussian noise. The table illustrates that as the number of projections increases, the reconstruction quality improves for all techniques. Consistent with visual assessments, LRIP-Net consistently ranks second across all three scanning configurations, while our proposed technique secures the top position.

The quantitative evaluations align with the observed visual quality. Our proposed technique achieves the highest PSNR of 30.9060, SSIM of 0.9724, and the lowest RMSE of 0.0285. These metrics substantiate the ability of our technique to preserve high-quality structures, mitigate noise, and minimize suboptimal label errors compared to ground truth data.

Furthermore, our method outperforms alternatives by attaining the highest PSNR and SSIM, coupled with the lowest RMSE. This dual validation, both quantitative and qualitative, underscores the efficacy of our approach in addressing the challenges associated with limited-angle reconstruction, particularly in terms of maintaining structural integrity.

(a) Unet reconstruction   (b) Proposed technique without Relative Variation   (c) Proposed technique including Relative Variation
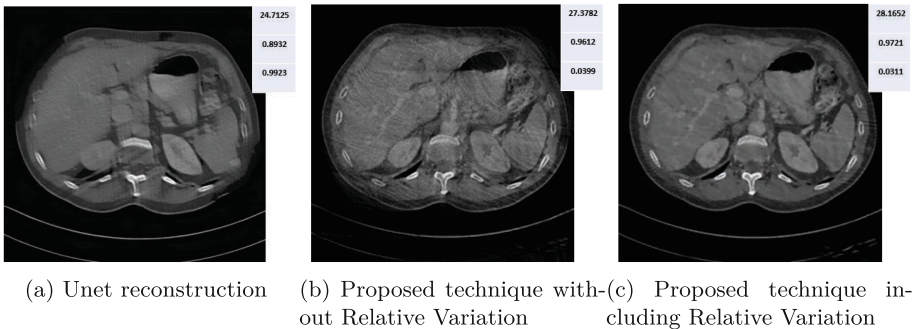
Fig. 5. ablation study

5   Ablation Study

We performed an ablation study to demonstrate how the proposed technique impacts reconstruction quality compared to the base U-Net. Initially, the base U-Net used FBP-reconstructed inputs, which resulted in very poor reconstruction quality. Instead, we propose using SART-TV reconstructed inputs to enhance the base U-Net architecture, thereby improving reconstruction quality.

The base U-Net's reconstructed output contained pattern-like noise, obstructing the visualization of small and thin structures. Figure 5 illustrates the performance of our proposed technique compared to the base U-Net. By providing SART-TV reconstructed inputs to the base U-Net, the reconstruction quality improves compared to using FBP-reconstructed inputs. However, as observed in Figure 5a, the U-Net's reconstruction quality remains poor due to its inability to reconstruct missing projection areas.

In contrast, our proposed technique without relative variation, shown in Figure 5b, successfully reconstructs the CT image in the missing projection areas, although it contains noise-like patterns that obscure the visualization of important organs. Finally, in Figure 5c, we utilize relative variation for structure decomposition, which removes these pattern-like artifacts and produces high-quality CT images with clear visualization of the organs.

Quantitative evaluation also suggests that including relative variation improves PSNR, SSIM, and RMSE to 28.1652, 0.9721, and 0.0311, respectively, compared to the base U-Net and the proposed technique without relative variation.

6   Conclusions

In this study, we introduce the Deep Prior Based RV-SART designed for reconstructing high-quality slices in extremely ill-posed conditions, particularly utilizing a 90-degree scanning angular range. Our approach incorporates prior information from a modified U-net with preprocessed input to feed the RV-SART algorithm about unmeasured data. Subsequently, it extracts structure from the initial reconstructed slice through structure-texture decomposition, facilitating the reconstruction of high-quality CT images while suppressing pattern-like artifacts.

Experiments demonstrate that Deep Prior Based RV-SART excels in high-quality reconstruction from limited-angle data, surpassing the performance of previous state-of-the-art techniques. Notably, prior information is constructed by adapting the efficient and simple architecture of sparse-based modified U-net for specific limited-angle data, providing crucial prior information regarding unmeasured data. This method not only sidesteps recent, computationally

complex deep learning approaches but also enhances accuracy in limited-angle reconstruction.

References

1. Adler, J., Öktem, O.: Learned primal-dual reconstruction. IEEE Trans. Med. Imaging **37**(6), 1322–1332 (2018)
2. Andersen, A.H., Kak, A.C.: Simultaneous algebraic reconstruction technique (sart): a superior implementation of the art algorithm. Ultrason. Imaging **6**(1), 81–94 (1984)
3. Baguer, D.O., Leuschner, J., Schmidt, M.: Computed tomography reconstruction using deep image prior and learned reconstruction methods. Inverse Prob. **36**(9), 094004 (2020)
4. Bappy, D., Kang, D., Lee, J., Baek, H.: Prior-based enhanced asd-pocs for artifact suppression and structural preservation in sparse-view cbct. In: Proceedings of the 39th ACM/SIGAPP Symposium on Applied Computing. pp. 496–505 (2024)
5. Boublil, D., Elad, M., Shtok, J., Zibulevsky, M.: Spatially-adaptive reconstruction in computed tomography using neural networks. IEEE Trans. Med. Imaging **34**(7), 1474–1485 (2015)
6. Bubba, T.A., Galinier, M., Lassas, M., Prato, M., Ratti, L., Siltanen, S.: Deep neural networks for inverse problems with pseudodifferential operators: An application to limited-angle tomography (2021)
7. Chen, G.H., Tang, J., Hsieh, J.: Temporal resolution improvement using piccs in mdct cardiac imaging. Medical physics **36**(6Part1), 2130–2135 (2009)
8. Chen, H., Zhang, Y., Chen, Y., Zhang, J., Zhang, W., Sun, H., Lv, Y., Liao, P., Zhou, J., Wang, G.: Learn: Learned experts' assessment-based reconstruction network for sparse-data ct. IEEE Trans. Med. Imaging **37**(6), 1333–1347 (2018)
9. Cheng, W., Wang, Y., Li, H., Duan, Y.: Learned full-sampling reconstruction from incomplete data. IEEE Transactions on Computational Imaging **6**, 945–957 (2020)
10. Ding, Q., Chen, G., Zhang, X., Huang, Q., Ji, H., Gao, H.: Low-dose ct with deep learning regularization via proximal forward-backward splitting. Physics in Medicine & Biology **65**(12), 125009 (2020)
11. Feldkamp, L.A., Davis, L.C., Kress, J.W.: Practical cone-beam algorithm. Josa a **1**(6), 612–619 (1984)

12. Gao, Q., Ding, R., Wang, L., Xue, B., Duan, Y.: Lrip-net: Low-resolution image prior-based network for limited-angle ct reconstruction. IEEE Transactions on Radiation and Plasma Medical Sciences **7**(2), 163–174 (2022)

13. Gao, Y., Liang, Z., Moore, W., Zhang, H., Pomeroy, M.J., Ferretti, J.A., Bilfinger, T.V., Ma, J., Lu, H.: A feasibility study of extracting tissue textures from a previous full-dose ct database as prior knowledge for bayesian reconstruction of current low-dose ct images. IEEE Trans. Med. Imaging **38**(8), 1981–1992 (2019)

14. Gonzales, B., Spronk, D., Cheng, Y., Tucker, A.W., Beckman, M., Zhou, O., Lu, J.: Rectangular fixed-gantry ct prototype: combining cnt x-ray sources and accelerated compressed sensing-based reconstruction. IEEE Access **2**, 971–981 (2014)

15. de Gonzalez, A.B., Darby, S.: Risk of cancer from diagnostic x-rays: estimates for the uk and 14 other countries. The lancet **363**(9406), 345–351 (2004)

16. Guo, Y., Zeng, L., Wang, C., Zhang, L.: Image reconstruction model for the exterior problem of computed tomography based on weighted directional total variation. Appl. Math. Model. **52**, 358–377 (2017)

17. Gupta, H., Jin, K.H., Nguyen, H.Q., McCann, M.T., Unser, M.: Cnn-based projected gradient descent for consistent ct image reconstruction. IEEE Trans. Med. Imaging **37**(6), 1440–1453 (2018)

18. Han, H., Gao, H., Xing, L.: Low-dose 4d cone-beam ct via joint spatiotemporal regularization of tensor framelet and nonlocal total variation. Physics in Medicine & Biology **62**(16), 6408 (2017)

19. Han, Y., Ye, J.C.: Framing u-net via deep convolutional framelets: Application to sparse-view ct. IEEE Trans. Med. Imaging **37**(6), 1418–1429 (2018)

20. Hu, D., Zhang, Y., Liu, J., Luo, S., Chen, Y.: Dior: Deep iterative optimization-based residual-learning for limited-angle ct reconstruction. IEEE Trans. Med. Imaging **41**(7), 1778–1790 (2022)

21. Jin, K.H., McCann, M.T., Froustey, E., Unser, M.: Deep convolutional neural network for inverse problems in imaging. IEEE Trans. Image Process. **26**(9), 4509–4522 (2017)

22. Kang, E., Min, J., Ye, J.C.: A deep convolutional neural network using directional wavelets for low-dose x-ray ct reconstruction. Med. Phys. **44**(10), e360–e375 (2017)

23. Lee, M., Kim, H., Kim, H.J.: Sparse-view ct reconstruction based on multi-level wavelet convolution neural network. Physica Med. **80**, 352–362 (2020)

24. Lin, W.A., Liao, H., Peng, C., Sun, X., Zhang, J., Luo, J., Chellappa, R., Zhou, S.K.: Dudonet: Dual domain network for ct metal artifact reduction. In: Proceedings of the IEEE/CVF Conference on Computer Vision and Pattern Recognition. pp. 10512–10521 (2019)

25. McCollough, C.H., Bartley, A.C., Carter, R.E., Chen, B., Drees, T.A., Edwards, P., Holmes, D.R., III., Huang, A.E., Khan, F., Leng, S., et al.: Low-dose ct for the detection and classification of metastatic liver lesions: results of the 2016 low dose ct grand challenge. Med. Phys. **44**(10), e339–e352 (2017)

26. Pelt, D.M., Batenburg, K.J.: Fast tomographic reconstruction from limited data using artificial neural networks. IEEE Trans. Image Process. **22**(12), 5238–5251 (2013)

27. Ronneberger, O., Fischer, P., Brox, T.: U-Net: Convolutional Networks for Biomedical Image Segmentation. In: Navab, N., Hornegger, J., Wells, W.M., Frangi, A.F. (eds.) MICCAI 2015. LNCS, vol. 9351, pp. 234–241. Springer, Cham (2015). https://doi.org/10.1007/978-3-319-24574-4_28

28. Siddon, R.L.: Fast calculation of the exact radiological path for a three-dimensional ct array. Med. Phys. **12**(2), 252–255 (1985)

29. Xu, J., Zhao, Y., Li, H., Zhang, P.: An image reconstruction model regularized by edge-preserving diffusion and smoothing for limited-angle computed tomography. Inverse Prob. **35**(8), 085004 (2019)
30. Xu, L., Yan, Q., Xia, Y., Jia, J.: Structure extraction from texture via relative total variation. ACM transactions on graphics (TOG) **31**(6), 1–10 (2012)
31. Yu, W., Zeng, L.: Iterative image reconstruction for limited-angle inverse helical cone-beam computed tomography. Scanning **38**(1), 4–13 (2016)
32. Yuan, H., Jia, J., Zhu, Z.: Sipid: A deep learning framework for sinogram interpolation and image denoising in low-dose ct reconstruction. In: 2018 IEEE 15th International Symposium on Biomedical Imaging (ISBI 2018). pp. 1521–1524. IEEE (2018)
33. Zhang, H., Dong, B., Liu, B.: Jsr-net: A deep network for joint spatial-radon domain ct reconstruction from incomplete data. In: ICASSP 2019-2019 IEEE International Conference on Acoustics, Speech and Signal Processing (ICASSP). pp. 3657–3661. IEEE (2019)